Draft version May 11, 2010
Preprint typeset using LaTeX style emulateapj v. 11/10/09

arXiv:0910.5025v2 [astro-ph.CO] 10 May 2010

IMPLICATIONS OF A HIGH ANGULAR RESOLUTION IMAGE OF THE SUNYAEV-ZEL'DOVICH EFFECT IN RXJ1347-1145

B. S. Mason[1,2], S.R. Dicker[3], P.M. Korngut[3], M.J. Devlin[3], W.D. Cotton[1], P.M. Koch[4], S.M. Molnar[4], J. Sievers[8], J.E. Aguirre[3], D. Benford[5], J.G. Staguhn[5,6], H. Moseley[5], K.D. Irwin[7], P.Ade[8]

Draft version May 11, 2010

ABSTRACT

The most X-ray luminous cluster known, RXJ1347-1145 ($z = 0.45$), has been the object of extensive study across the electromagnetic spectrum. We have imaged the Sunyaev-Zel'dovich Effect (SZE) at 90 GHz ($\lambda = 3.3$ mm) in RXJ1347-1145 at $10''$ resolution with the 64-pixel MUSTANG bolometer array on the Green Bank Telescope (GBT), confirming a previously reported strong, localized enhancement of the SZE $20''$ to the South-East of the center of X-ray emission. This enhancement of the SZE has been interpreted as shock-heated (> 20 keV) gas caused by an ongoing major (low mass-ratio) merger event. Our data support this interpretation. We also detect a pronounced asymmetry in the projected cluster pressure profile, with the pressure just east of the cluster core $\sim 1.6\times$ higher than just to the west. This is the highest resolution image of the SZE made to date.

Subject headings: galaxies: clusters: individual (RXJ1347-1145); cosmology: observations; cosmic microwave background; GBT

1. INTRODUCTION

The rich cluster RXJ1347-1145 ($z = 0.45$) is the most X-ray luminous galaxy cluster known (Schindler et al. 1995, 1997; Allen et al. 2002) and has been the object of extensive study at radio, millimeter, submillimeter, optical and X-ray wavelengths (Kitayama et al. 2004; Komatsu et al. 2001; Gitti et al. 2007; Allen et al. 2002; Schindler et al. 1997; Pointecouteau et al. 1999; Ota et al. 2008; Cohen & Kneib 2002; Bradač et al. 2008; Miranda et al. 2008). Discovered in the ROSAT All-Sky Survey, RXJ1347-1145 was originally thought to be a dynamically old, relaxed system (Schindler et al. 1995, 1997) based on its smooth, strongly-peaked X-ray morphology— a prototypical relaxed "cooling-flow" cluster. The NOBA 7 bolometer system on the 45-meter Nobeyama telescope (Kitayama et al. 2004; Komatsu et al. 2001) has made high-resolution observations ($13''$ FWHM, smoothed to $\sim 19''$ in the presented map) of the Sunyaev-Zel'dovich effect (SZE) at 150 GHz which indicate a strong enhancement of the SZ effect $20''$ (170 kpc) to the south-east of the peak of the X-ray emission, however. Hints of this asymmetry had been seen in earlier, lower resolution measurements with the Diabolo 2.1 mm photometer on the IRAM 30-m (Pointecouteau et al. 1999). The enhancement has been interpreted as being due to hot ($T_e > 20$ keV) gas which is more difficult to detect using X-rays than cooler gas is, owing to the lower responsivities of imaging X-ray telescopes such as Chandra and XMM at energies above ~ 10 keV. In contrast, the SZE intensity is proportional to T_e up to arbitrarily high temperatures, aside from relativistic corrections which are weak at 90 GHz, so such hot gas stands out. The feature is consistent with the presence of a large substructure of gas in the intra-cluster medium (ICM) shock-heated by a merger, as is seen in the "Bullet Cluster" 1E0657-56 (Markevitch et al. 2002); this interpretaion has been supported by more recent observations (e.g. Allen et al. 2002; Ota et al. 2008). *Thus, rather than being an example of a hydrostatic, relaxed system, high-resolution SZE observations suggest that the observed properties of the ICM in RXJ1347-1145 are strongly affected by an ongoing merger.* This is a striking cautionary tale for ongoing blind SZE surveys (Carlstrom et al. 2002), for which useful X-ray data will be difficult or impossible to obtain for many high-z systems, as well as a sign that our current understanding of nearby, well-studied X-ray clusters may be dramatically incomplete.

Reports (Komatsu et al. 2001; Pointecouteau et al. 2001; Kitayama et al. 2004) of a strong enhancement of the SZE away from the cluster center are based on relatively low-resolution images compared to the size of the offsets and features involved. SZE images at lower frequencies also show show substantial offsets between the peak of X-ray and SZE emission; for instance, the 21 GHz (Komatsu et al. 2001) and SZE peak is $\sim 20''$ to the SE of the X-ray peak, and the 30 GHz (Reese et al. 2002) SZE peak is $\sim 13''$ to the SE of the X-ray peak. The situation is further complicated by the presence of a radio source in the center of the cluster. We have sought to test these claims, and to begin to untangle the astrophysics of this interesting system, with higher resolution imaging at a complementary frequency. In this paper we present the highest angular resolution image of the SZE yet made. We observed RXJ1347-1145 with the MUSTANG 90 GHz bolometer array on the Robert C. Byrd Green Bank Telescope (GBT). At the redshift of

[1] National Radio Astronomy Observatory, 520 Edgemont Rd. Charlottesville VA 22903, USA
[2] contact author: bmason@nrao.edu
[3] University of Pennsylvania, 209 S. 33rd St., Philadelphia, PA 19104, USA
[4] Institute of Astronomy and Astrophysics, Academia Sinica. P.O. Box 23-141, Taipei 10617, Taiwan, R.O.C.
[5] NASA Goddard Space Flight Center, Greenbelt, MD 20771, USA
[6] Johns Hopkins U, Dept. of Physics & Astronomy, 3400 N. Charles St, Baltimore, MD 21218, USA
[7] National Institute of Standards and Technology, 325 Broadway, Boulder, CO 80303, USA
[8] School of Physics and Astronomy, Cardiff University, 5 The Parade, Cardiff, CF24 3AA, UK

the cluster (and assuming $\Omega_\Lambda = 0.3, \Omega_{tot} = 1, h = 0.73$) the GBT+MUSTANG 9″ beam corresponds to a projected length of 54 kpc. The observations are described in § 2 and the data reduction in § 3. Our interpretation and conclusions are presented in § 4.

2. INSTRUMENT & OBSERVATIONS

MUSTANG is a 64 pixel TES bolometer array built for use on the 100-m GBT (Jewell & Prestage 2004). MUSTANG uses reimaging optics with a pixel spacing of $0.63f\lambda$, operates in a bandpass of 81–99 GHz, and is cooled by a pulse tube cooler and Helium-4/Helium-3 closed cycle refrigerator. Further technical details about MUSTANG can be found in Dicker et al. (2006, 2008). More detailed information is also provided about MUSTANG, the observing strategy, and the data analysis algorithms in Cotton et al. (2009) and Dicker et al. (2009), which present the results of other early MUSTANG observations. Further information can be obtained at the MUSTANG web site[9].

The observations we present were collected in two runs, one on 21 Feb. 2009 and one on 25 Feb. 2009, each approximately four hours in duration including time spent setting up the receiver and collecting calibration observations. For both runs the sky was clear with ~ 6 mm of precipitable water vapor, corresponding to ~ 20 K zenith atmospheric loading at 3.3 mm. Both were night-time sessions, important because during the day variable gradients in the telescope structure's temperature degrade its 90 GHz performance significantly. The telescope focus was determined by collecting small maps of a bright calibrator source at a range of focus settings; every 30-40 minutes throughout the session the beam is checked on the calibrator. Typically the required focus corrections are stable to a few millimeters over several hours once residual daytime thermal gradients have decayed.

Once the focus was established, the in-focus and out-of-focus beam maps were used to solve for primary aperture wavefront phase errors using the "Out-of-Focus" (OOF) holography technique described by Nikolic et al. (2007). The solutions were applied to the active surface. This procedure improves the beamshape and increases the telescope peak forward gain, typically by $\sim 30\%$. This approach is effective at correcting phase errors on scales of 20 meters or larger on the dish surface, but is not sufficiently sensitive to solve for smaller scales. Therefore there are residual uncorrected wavefront errors that result in sidelobes out to $\sim 40''$ from the main beam. Deep beam maps were collected on the brightest 90 GHz sources on several occasions, principally in test runs on 24/25 March 2009. The repeatability of the GBT 90 GHz beam after application of the OOF solutions was found to be good. The analysis of the beam map data is discussed in § 3.1.

Maps of RXJ1347-1145 (J2000 coordinates $13h47m30.5s$, $-11°45'09''$) were collected with a variety of scan patterns designed to simultanously maximize on-source time and the speed at which the telescope moved when crossing the source. The effects of atmospheric and instrumental fluctuations, which become larger on longer timescales, are reduced by faster scan speeds. The primary mapping strategies were: a) a "daisy" or "spirograph" scan in which the source of interest is frequently recrossed; and b) a "billiard ball" scan, which moves at an approximately constant speed and has more uniform coverage over a square region of interest. The nominal region of interest in this case was $5' \times 5'$, centered on RXJ1347-1145. The size of the maps is sufficiently small that except under the most exceptionally stable conditions, instrument and random atmosphere drifts dominate the constant atmosphere (sec(za)) term and any possible ground pickup. The total integration time on source was 3.4 h.

The asteroid Ceres was observed on both nights and used as the primary flux calibrator assuming $T_B = 148$ K (T. Mueller, private comm.). We assign a 15% uncertainty to this calibration. We checked the Ceres calibration on nights when other sources (Saturn, CRL2688) were visible and found consistent results to within the stated uncertainty. Using these observations and the lab-measured receiver optical efficiency of $\eta_{opt,rx} = 50 \pm 10\%$ we compute an overall aperture efficiency of $\eta_{aperture,gbt} = 20\%$, corresponding to a Ruze-equivalent surface RMS of 315μm. This result is consistent with recent traditional holographic measurements of the GBT surface. Since the observations presented here the surface has been set based on further holography maps and now has a surface RMS, weighted by the MUSTANG illumination pattern, of $\sim 250\mu$m.

3. DATA REDUCTION

3.1. *Beam Characterization*

Imaging diffuse, extended structure requires a good understanding of the instrument and telescope beam response on the sky. To achieve this we collected numerous beam maps through our observing runs, including several deep beammaps on bright (5 Jy or more) sources. After applying the Out-of-Focus holography corrections to the aperture the beam results were repeatable; Figure 1 shows the radial beam profile from maps of a bright source (3C279) collected on two occasions. We find a significant error beam concentrated around the main lobe which increases the beam volume from 87 arcsec^2 (for the core component only) to 145 arcsec^2. We attribute this beam to residual medium and small scale phase errors on the primary aperture. The beam shape and volume is taken into account when comparing to model predictions. By way of comparison, Figure 1 also shows the profile of the beam determined from the radio source in the center of RXJ1347-1145. Since the SZ map has been smoothed, the apparent beam is slightly broader, but allowing for this, still consistent with the beam determined on 3C279.

3.2. *Imaging*

A number of systematic effects must be taken into account in the time domain data before forming the image:

1. The responsivities of individual detectors are measured using an internal calibration lamp that is pulsed periodically. Optically non-responsive detectors (10-15 out of 64) are flagged for removal from subsequent analysis. Typical detector responsivities are stable to $2-3\%$ over the course of several hours.

[9] http://www.gb.nrao.edu/mustang/

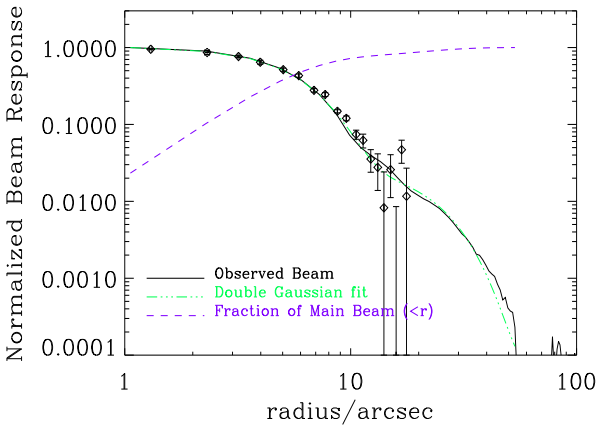

FIG. 1.— MUSTANG+GBT beams determined from observations of 3C279. The green dash triple-dot line shows a double-Gaussian fit to the observed beam. The purple dashed line is the cumulative fractional beam volume. We attribute the excess power in the wings of the observed beam to residual medium and small scale phase errors on the dish. The data points (diamonds with error bars) show a complementary determination of the beam from the 5 mJy radio source in the center of RXJ1347-1145. The beam in this case is slightly wider due to the smoothing (4" FWHM) applied to the final map, which is accounted for in the analysis.

2. Common mode systematic signals are subtracted from the data. These are caused by atmospheric and instrumental (thermal) fluctuations. The pulse tube cooler, which provides the 3K base temperature of the receiver, induces a 1.4 Hz signal due to small emission fluctuations of the 3K optics. The pulse-tube signal is removed by fitting and subtracting a 1.41 Hz sine wave. The remaining common mode signal is represented by a template formed by a weighted average of data from good pixels; this template is low-pass filtered and subtracted from the data, with a fitted amplitude per detector. The low-pass filter time constant (typically 0.1 Hz) is determined by the stability of the data in question. This procedure helps to preserve large-scale structure in the maps.

3. Slow residual per-pixel drifts are removed using low-order orthogonal polynomials.

4. Individual detector weights are computed from the residual detector timestreams after the above steps. Since the noise level of the detectors varies considerably this is an important step. Best results are obtained by retaining only the top $\sim$ 80% of responsive detectors.

5. The remaining calibrated detector timestreams are inspected visually on a per-scan (typically 5 minute period) basis. Scans which have timestreams with obvious, poorly-removed systematic signals remaining are removed. This results in flagging 28% of scans. The SNR in an individual detector timestream is sufficiently low that this does not bias our map.

Following these calibration steps the detector timestream data are gridded onto a 2″ pixellization in Right Ascencion and Declination using a cloud-in-cell gridding kernel.

To check our results we have implemented three, mostly independent analysis pipelines. The results in this paper are based on a straightforward but flexible single-pass pipeline written in IDL, described above. There is also an iterative, single-dish CLEAN based approach implemented in the OBIT package (Cotton 2008) and an optimal SNR method in which the time domain data are decomposed into noise (covariance) eigenvectors; their temporal power spectra computed; and a maximum likelihood map constructed from the noise-weighted eigenvectors. Results obtained with these algorithms were consistent. The first two approaches are described in more detail in Dicker et al. (2009).

Our final map, smoothed by a 4″ FWHM Gaussian and gridded on 0″.5 pixels, is shown in Figure 2, along with the difference between the two individual night maps. It shows a strong, clear SZ decrement, well separated from the central point source and consistent with the level expected from the Kitayama et al. (2004, hereafter K04) 150 GHz measurement. The right hand panel shows the image formed by differencing the images of the two individual nights. By computing the RMS in a fiducial region in the center of the difference image (and scaling down by a factor of 2 to account for the differencing and the shorter integration times) we estimate a map-center image noise of $\sim 0.3\,$mJy/bm (rms). The noise level in regions of the map outside the fiducial region is corrected for exposure time variations assuming Gaussian, random noise with a white power spectrum. The enhancement of the SZE to the south east of the X-ray peak, originally detected by Komatsu et al. at 4.2σ significance, is confirmed by our measurement at 5.4σ (indicating the peak SNR per beam) with a factor of ~ 2 greater angular resolution.

A detailed assessment of the impact of this is presented in § 3.3. Work is underway to develop analysis techniques which account for correlated noise in a way that permits quantitative model fitting.

3.3. *Simulations*

It is difficult to measure diffuse, extended structure such as the SZE, particularly in the presence of potentially contaminating systematic signals such as time-varying atmospheric fluctuations. To assess the impact of residual, unmodelled noise fluctuations in the maps we have undertaken an extensive suite of simulations which replace the raw detector timestream data with simulated data. As a source for the simulated data we used real detector timestreams collected during observations of a blank patch of sky collected for another project. The phase of these timestreams with respect to the telescope trajectory on RXJ1347-1145 was randomly shifted to create different instances of noisy cluster observations. We added simulated astronomical signals as described below in order to determine how well the (known) input signals are recovered in the maps.

To assess the spatial fidelity of our reconstructed images, random white-noise skies were generated on 2″ grids, subsequently smoothed by a 9″ (FWHM) Gaussian. These skymaps served as input to generate fake timestreams which were then processed by the exact processing scripts used to produce the image in Figure 2. The ratio of the absolute magnitude of the Fourier transform of the reconstructed sky map to the absolute mag-

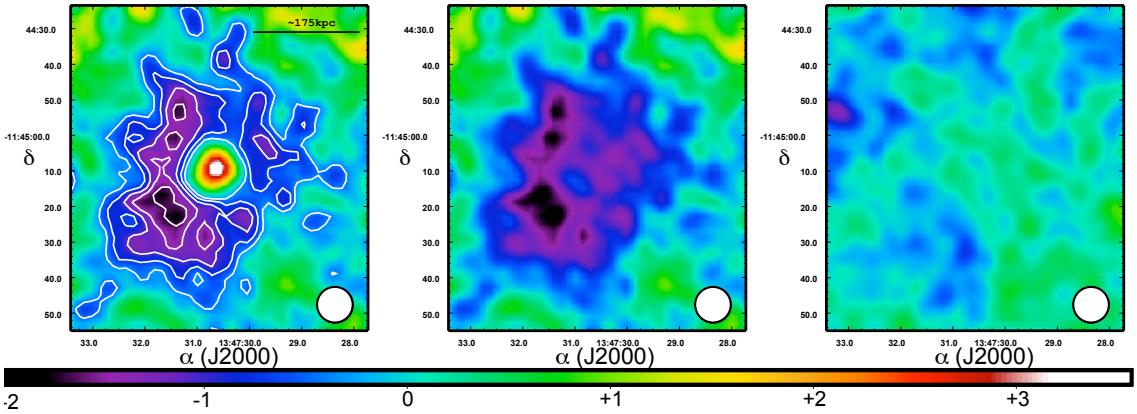

FIG. 2.— MUSTANG image of the SZE in RXJ1347-1145 (left); the same, with the point source subtracted as described in the text (center); and the individual nights imaged separately and differenced, on the same color scale (right). The noise in the center of the map is is $\sim 0.3\,$mJy/bm; contours in the left panel correspond to SNR of 1 to 5 in 1σ increments and account for variations in integration time in the map, so are not directly proportional to the image. Color scale units are mJy/bm. The MUSTANG beam ($10''$ FWHM after smoothing) is shown in the lower right of each panel.

nitude of the Fourier transform of the input skymap measures the fidelity of our image reconstructions as a function of angular scale. The results of repeating this 100 times, with different white-noise skies and noise instances, are shown in Figure 4. We find that our pipeline faithfully recovers structures up to 60″, with reasonable response but some loss of amplitude on larger scales, up to 120″. The loss of structure on small angular scales is an effect of our relatively coarse pixellization. Simulations were carried out at similar signal to noise ratios as those in our final map, although changes in the signal to noise ratio of over a factor of 5 showed no significant change to our transfer function

The common-mode subtraction, essential to removing atmospheric and instrumental systematic signals, can also introduce negative bowls around bright point sources which could mimic the SZE in cases such as RXJ1347-1145. To determine the magnitude of this systematic we have followed a similar approach. Instead of white-noise skies the input signal consists of a single unresolved source with a flux density of 5 mJy at the location of the radio source seen in RXJ1347-1145. The resulting negative bowl in the reconstructed images has a mean peak spurious decrement $\sim 2\%$ of the point source peak brightness, in comparison with $\sim 50\%$ for our real data. Additionally the iterative pipeline (OBIT) is much less susceptible to such artifacts, and shows consistent results. We conclude that this is not a significant contribution to our result.

3.4. *Image Domain Noise Estimate*

We divide the data set in half and subtract the individual night images to obtain a difference map. The RMS of this difference map in the central 85 by 93 arcseconds, dividing by two to correct for the differencing and the reduced integration time in each individual night image, gives an image noise level of 0.3 mJy. A histogram of the pixel values in this region of the difference image is shown in figure 3.

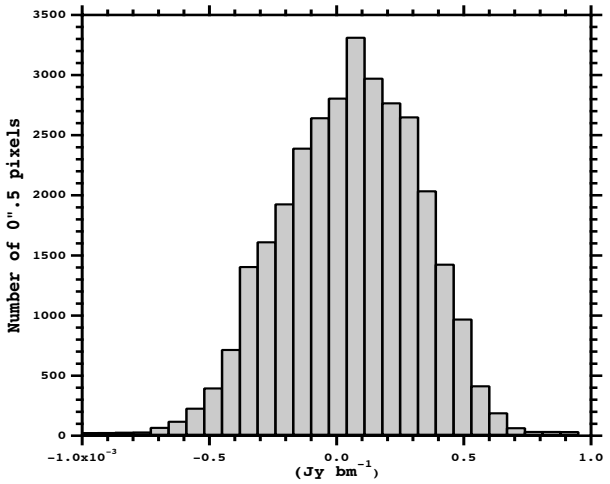

FIG. 3.— Histogram of pixel values in the difference image in Figure 2. The histogram is well described by a gaussian distribution of $1\sigma = 0.3$ mJy/bm

We obtain a complementary estimate of the noise from a region of the final SZ map well away from the cluster. Correcting for the difference in integration times in these regions of the map, this result is consistent to within 8%.

Using this noise figure, the peak SNR per beam in the map— on the SZE decrement SE of the cluster core— is 5.4σ. More aggressive filtering the map results in an even higher detection significance for the SE enhancement by reducing the low spatial frequency tail of the noise power spectrum (Figure 4).

3.5. *The Effects, and Subtraction, of the Central Radio Source*

Our final map has sufficient angular resolution to distinguish the central radio source from the structures of interest. In particular it is clear that, as seen in earlier analyses of the SZE in this cluster (Pointecouteau et al. 1999) there is a strong azimuthal variation in the intensity of the SZE at a radius of $\sim 20''$ from the X-ray centroid, which also coincides with the radio source.

To produce a source-subtracted image we fit and subtract an azimuthally symmetric, double-Gaussian beam (as determined from 3C279 in § 3.1). The reason for assuming azimuthal symmetry is that the hour angle sampling of the 3C279 data is considerably more limited than that of the RXJ1347-1145 data; therefore the 3C279 data will not provide a good measurement of the effective two-dimensional beam, only of its average radial profile. Furthermore the SNR on the point source in RXJ1347-1145 is insufficient to measure significant departures from azimuthal symmetry.

The average radial profile of the central source in RXJ1347-1145 is shown in Figure 1 out to $r = 15''$, where the signal becomes too weak to measure above thermal noise and variations in the SZE.

3.6. *Effect of Background Anisotropies*

The angular scales reconstructed in our map ($\sim 1'.5$ and smaller) correspond to spherical harmonic multipoles of $\ell = 7200$ and higher. On these scales intrinsic CMB anisotropies are strongly suppressed by photon diffusive damping at the last scattering surface and do not contribute measurably to our result at the sensitivity level we have achieved.

4. INTERPRETATION & CONCLUSIONS

4.1. *Comparison with Previous SZE Observations*

Figure 5 presents a direct comparison of the MUSTANG and NOBA results in units of main-beam averaged Compton y parameter. For a more accurate comparison, we downgrade the resolution and pixelscale of the MUSTANG map to match that of NOBA (13" FWHM on a 5" pixel grid). The overall agreement between the maps is excellent, in particular as regards the amplitude and morphology of the local enhancement of the SZE south-east of the cluster core. The largest discrepancy is south west of the cluster, where NOBA shows a 3σ compact decrement which is absent from the MUSTANG data. Considering the low and uniform X-ray surface brightness in the vicinity of this discrepancy (see Figure 7) and the higher angular resolution and lower noise of the MUSTANG data, it is likely that this feature is a spurious artifact in the NOBA map. Both datasets also show a ridge extending north from the shock front on the eastern side of the cluster. In the 150 GHz map

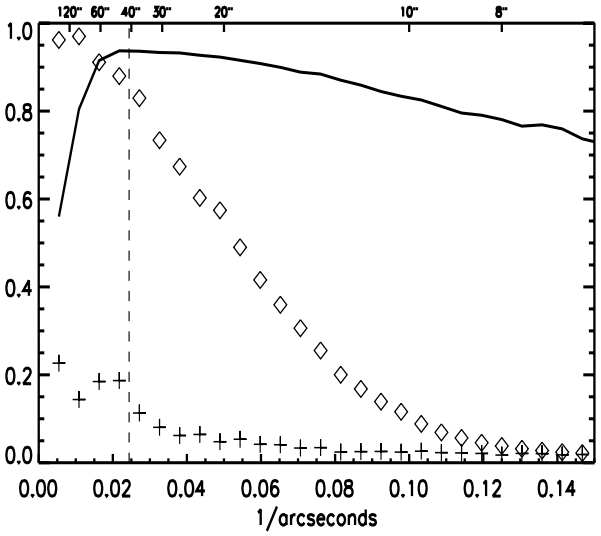

FIG. 4.— Map noise characteristics. *Solid curve*: The ratio of the absolute magnitude of the Fourier transform of the input map to the absolute magnitude of the Fourier transform of the output map from simulations. All structure on scales smaller than $1'$ was recovered well although there is a fall off towards high spatial frequencies due to pixellization effects. *Diamonds*: The absolute magnitude of the Fourier transform of the (reconstructed simulated) cluster map, normalized to a peak value of unity. *Plus marks*: Absolute magnitude of the fourier transform of signal-free simulated maps, with the same normalization as the cluster data. The dashed line shows the size of the MUSTANG instantaneous field of view.

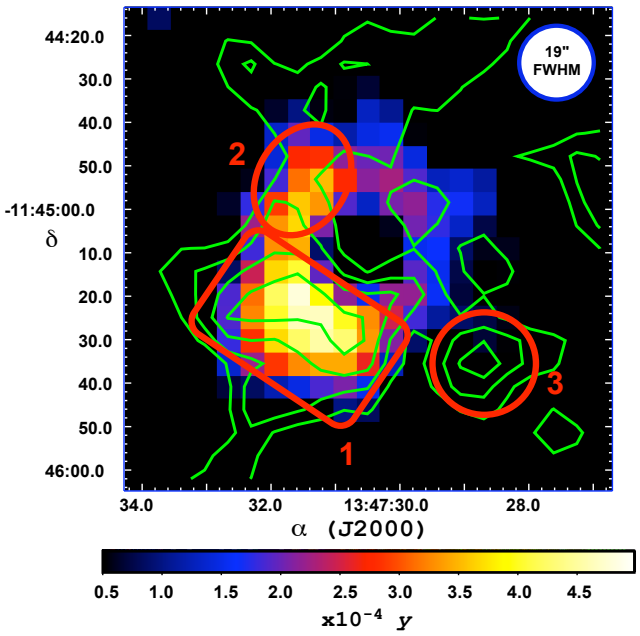

FIG. 5.— Comparison of NOBA and Mustang maps of RX J1347-1145. The color scale shows the MUSTANG data with 5″ pixels, smoothed to match the published NOBA map resolution. The contours show the NOBA map at intervals of 1.16×10^{-4} in y starting from 5×10^{-5}. Three labeled features are discussed in the text: *1*, the hot shock south-east of the cluster core; *2*, an enhancement in integrated pressure to the east; and *3*, a compact decrement observed at $\sim 3\sigma$ by NOBA that is absent from the MUSTANG image.

the feature is of marginal significance $(1 - 2\sigma)$; interestingly, it is clearly visible in the 350 GHz SZE increment map but K04 dismiss it due to the possibility of confusing dust emission from the nearby galaxies.

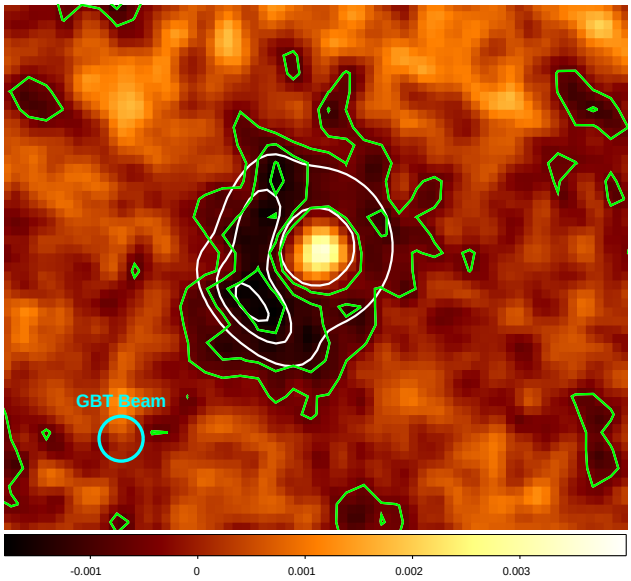

FIG. 6.— MUSTANG SZE image of RXJ1347-1145 with contours (thin green lines) at −1.5, −1.0, and −0.5 mJy/bm. The bold white contours, at the same surface brightness levels, show the model SZ signal discussed in the text.

4.2. *Empirical Model of the SZE in RXJ1347-1145*

We construct a simple empirical model for the cluster SZE assuming the isothermal β-model of Schindler et al. (1997) normalized by the SZE measurement of Reese et al. (2002) and Kitayama et al. (2004) to describe the bulk cluster emission. We add a 5 mJy point source in the cluster core, coincident with the peak of the β-model, and two Gaussian components in integrated pressure, one south-east and one almost directly east of the cluster center. In comparing to our 90 GHz data, we use the relatavistic correction of Sazonov & Sunyaev (1998), assuming $kT = 25\,\mathrm{keV}$ (which reduces the amplitude of the decrement by 15%) for the Gaussian components and $kT = 10\,\mathrm{keV}$ for the bulk component. The parameters chosen (two Gaussian widths for each component, a position, a peak surface brightness, and a position angle) are shown in Table 1. The resulting sky image is convolved with our PSF (§ 3.1) and transfer function (§ 3.3). We find that this provides a good match to the data (Figure 6). The peak comptonization at 10″ Gaussian resolution is 3.9×10^{-4} on the eastern ridge and 6.0×10^{-4} on the region identified as a shock by Komatsu et al. When convolved to 19″ FWHM (NOBA) resolution, we find $\Delta y = 3.9 \times 10^{-4}$, close to their observed value $\Delta y = 4.1 \times 10^{-4}$. The intent of this static, phenomenological model is simply to provide a description of the observed high angular-resolution SZE and a direct comparison of NOBA and MUSTANG results. Work is underway which will allow quantitatively determining the best fit physical model by simulataneously fitting datasets at multiple wavelengths using a Monte-Carlo Markov Chain. This work is beyond the scope of this paper and will be presented in a follow up publication.

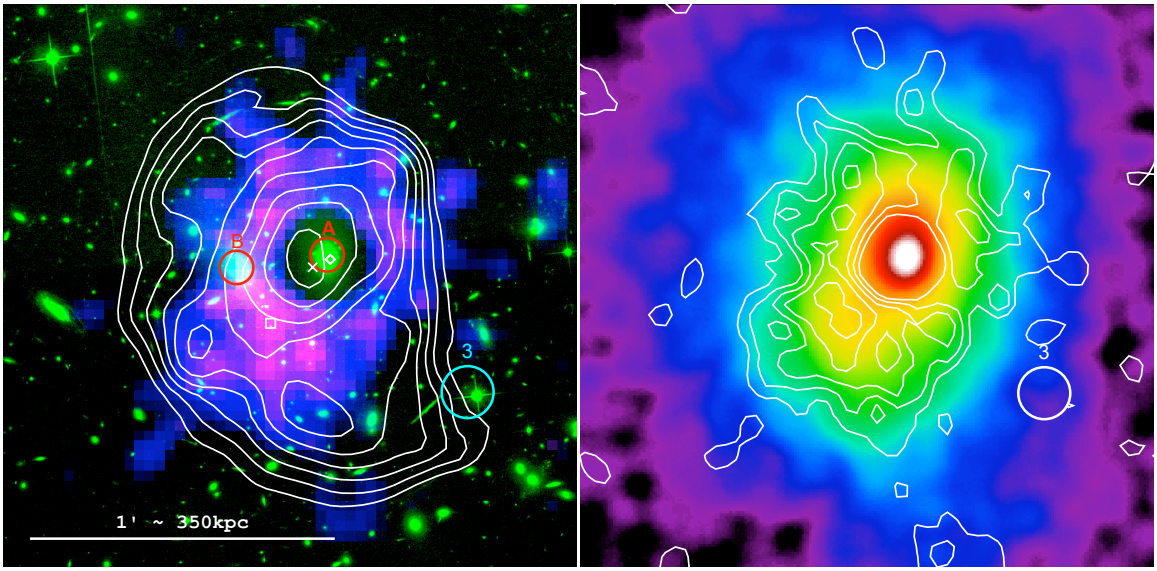

FIG. 7.— **Left:** False color composite Image of RXJ1347-1145. Red/blue: Mustang SZ. Green: Archival HST/ACS image taken through the F814W filter; and white contours: Surface mass density κ from the weak + strong lensing analysis of Bradač et al. (2008). Contours are linearly spaced in intervals of $\Delta\kappa = 0.1$ beginning at $\kappa = 1.0$. Several features are labelled: *A* indicates the central BCG, which is a radio source; *B* indicates the BCG of the secondary cluster; and *3* (also labeled in the right-hand panel) indicates the location of the discrepancy between NOBA and MUSTANG, discussed in the text and Figure 5. The diamond, cross and box mark the locations of the peaks in X-ray surface brightness, surface mass density and SZE decrement respectively. **Right:** Contours of the MUSTANG decrement SNR (1σ to 5σ in 1σ increments) superposed on the Chandra count-rate image smoothed to $10''$ resolution.

Component	Amplitude $[y/10^{-3}]$	Offset $['']$	Notes
β-model	1.0	0, 0	$\theta_c = 10''$, $\beta = 0.60$
Shock	1.6	-14, 14	$\sigma_1 = 8''$, $\sigma_2 = 2''$, P.A. $= 45°$
Ridge	1.0	10, 14	$\sigma_1 = 8''$, $\sigma_2 = 2''$, P.A. $= -15°$

TABLE 1
NOTE: OFFSET IS (NORTH,EAST) OF PEAK X-RAY POSITION

4.3. *Multi-wavelength Phenomenology*

Our data show an SZE decrement with an overall significance of 5.4σ. At the center of the cluster, coincident with the peak of X-ray emission and the brightest cluster galaxy (BCG), there is an unresolved 5 mJy radio source. This flux density is consistent with the 90 GHz flux density presented in Pointecouteau et al. (2001), as well as what is expected from a power law extrapolation of 1.4 GHz and 30 GHz measurements (Condon et al. 1998; Reese et al. 2002). A strong, localized SZE decrement can be seen $20''$ to the south-east of the center of X-ray emission and clearly separated from the cluster center. Our data also indicate a high-pressure ridge immediately to the east of the cluster center.

K04 tentatively attribute the south-east enhancement to a substructure of gas 240 ± 183 kpc in length along the line of sight, at a density (assumed uniform) of $(1.4 \pm 0.59) \times 10^{-2}\,\mathrm{cm}^{-3}$ and with a temperature $T_e = 28.5 \pm 7.3$ keV. Recent X-ray spectral measurements (Ota et al. 2008) with SUZAKU also indicate the presence of hot gas in the south-east region ($T_e = 25.1^{+6.1}_{-4.5}\ ^{+6.9}_{-9.5}$ keV with statistical and systematic errors, respectively, at 90% confidence level). Allen et al. (2002) have reported that the slight enhancement of softer X-ray emission in this region seen by Chandra is consistent with the presence of a small substructure of hot, shocked gas. Kitayama et al. (2004) attribute the hot gas to an ongoing merger in the plane of the sky. The merger hypothesis is supported by optical data, in particular, the presence of a second massive elliptical $\sim 20''$ directly to the east of the BCG that coincides with the center of X-ray emission (and with the radio point source). Furthermore the density and temperature of the hot substructure indicate that it is substantially overpressured compared to the surrounding ICM. Assuming a sound speed of 1600 km/sec this overpressure region should relax into the surrounding ICM on a timescale ~ 0.1 Gyr, again arguing for an ongoing merger.

Our data support this merger scenario. To put them in context, Figure 7 shows a composite image with archival Chandra and HST data, and the weak + strong lensing mass map of Bradač et al. (2008). We propose that the data are best explained by a merger occuring in or near the plane of the plane of the sky. The left-hand ("B") cluster, having fallen in from the south-*west*, has just passed closest approach and is hooking around to the north-west. As the clusters merge shock forms, heating the gas in the wake of its passage. As argued by Kitayama et al. (2004), and seen in simulations (Takizawa 1999), the clusters must have masses within a factor of 2 or 3 of equality and a substantial ($\sim$ 4000 km/sec) relative velocity in order to produce the high observed plasma temperatures, $T_e > 20$ keV. This merger geome-

try is consistent with the lack of structure in the line-of-sight cluster member galaxies' velocities (Cohen & Kneib 2002). The primary (right-hand, "A") cluster contains significant cold and cooling gas in its core (a "cooling flow"). Such gas is seen to be quite robust in simulated major cluster mergers (Gómez et al. 2002; Poole et al. 2008). Even in cases where the cooling flow is finally disrupted by the encounter, Gómez et al. (2002) find a delay of $1-2$ GYr between the initial core encounter and the collapse of the cooling flow. The existence of a strong cooling flow, therefore, does not argue against a major merger in this case. More detailed simulations could shed further light on this interesting system.

4.4. *Broad Implications*

Since calibrating SZ observable - mass relationships is vital to understand the implications of ongoing SZE surveys, it is important to understand the mechanism by which a substantial portion of the ICM can be heated so dramatically, and how this energy is distributed through the ICM over time. Observations of cold fronts in other clusters (e.g. Vikhlinin et al. 2001) have shown that energy transport processes in the ICM are substantially inhibited, perhaps by magnetic fields. It is distinctly possible, then, that once heated by shocks, very hot phases would persist.

We have estimated the magnitude of the bias in an arcminute-resolution Compton y measurement that is introduced by a hot gas phase by convolving the two gaussian components of the SZE model in Table 1 with a $1'$ FWHM Gaussian beam, typical of SZ survey telescopes such as ACT (Swetz et al. 2008; Hincks et al. 2009) or SPT (Staniszewski et al. 2008; Vanderlinde et al. 2010). Compared with the bulk emission component, also convolved with a $1'$ beam, the small-scale features are a 10% effect. While relatively modest this is a systematic bias in the Compton y parameter which, if not properly accounted for, would result in a 20% overestimate in distances (underestimate in H_0) derived from a comparison of the SZE and X-ray data which did not allow for the presence of the hot gas component. To assess the impact on the *scatter* in $M-y$, a larger sample of high-resolution SZE measurements is needed. A full calculation would also need to take into consideration effects such as detection apertures and the spatial filtering due to imaging algorithms, some of which would increase the importance of the effect and some of which would decrease its importance.

This is the one of a very few clusters that has been observed at sub-arcminute resolution in the SZE (see also Nord et al. 2009), so it is possible that many clusters exhibit similar behavior. Such events, if their enhancement of the SZE brightness is transient, could also bias surveys towards detecting kinematically disturbed systems near the survey detection limits. The astrophysics that has been revealed by high resolution X-ray observations, and is beginning to be revealed by high resolution SZE data, is interesting in its own right. The SZE observations require large-aperture millimeter telescopes which have henceforth been lacking, but with both large single dishes and ALMA coming online, exciting observations will be forthcoming. There is substantial room for improvement: since the observations we report here the GBT surface has improved from 320μm RMS to 250μm RMS, which will yield more than a factor of 1.5 improvement in sensitivity. The array used in these observations, while state of the art, has not yet achieved sky photon noise limited performance; further progress is being made in this direction. Considering these facts, and that the results presented here were acquired in a short period of allocated telescope time (8h), this new high-resolution probe of the ICM has a bright future.

The National Radio Astronomy Observatory is a facility of the National Science Foundation operated under cooperative agreement by Associated Universities, Inc. We thank Eiichiro Komatsu for providing the NOBA SZ map; Marusa Bradac for providing her total mass map; Masao Sako, Ming Sun, Maxim Markevitch, Tony Mroczkowski and Erik Reese for helpful discussions; and Rachel Rosen and an anonymous referee for comments on the manuscript.

REFERENCES

Allen, S. W., Schmidt, R. W., & Fabian, A. C. 2002, MNRAS, 335, 256

Bradač, M., Schrabback, T., Erben, T., McCourt, M., Million, E., Mantz, A., Allen, S., Blandford, R., Halkola, A., Hildebrandt, H., Lombardi, M., Marshall, P., Schneider, P., Treu, T., & Kneib, J. 2008, ApJ, 681, 187

Carlstrom, J. E., Holder, G. P., & Reese, E. D. 2002, ARA&A, 40, 643

Cohen, J. G. & Kneib, J.-P. 2002, ApJ, 573, 524

Condon, J. J., Cotton, W. D., Greisen, E. W., Yin, Q. F., Perley, R. A., Taylor, G. B., & Broderick, J. J. 1998, AJ, 115, 1693

Cotton, W. 2008, PASP, 120, 439

Cotton, W. D., Mason, B. S., Dicker, S. R., Korngut, P. M., Devlin, M. J., Ade, P. A. R., Aguirre, J., Ames, T. J., Benford, D. J., Chen, T. C., Chervenak, J. A., , Figueroa-Feliciano, E., Irwin, K. D., Maher, S., Mello, M., & Moseley, S. H. 2009, submitted to ApJ

Dicker, S. R., Abrahams, J. A., Ade, P. A. R., Ames, T. J., Benford, D. J., Chen, T. C., Chervenak, J. A., Devlin, M. J., Irwin, K. D., Korngut, P. M., Maher, S., Mason, B. S., Mello, M., Moseley, S. H., Norrod, R. D., Shafer, R. A., Staguhn, J. G., Talley, D. J., Tucker, C., Werner, B. A., & White, S. D. 2006, in Presented at the Society of Photo-Optical Instrumentation Engineers (SPIE) Conference, Vol. 6275, Society of Photo-Optical Instrumentation Engineers (SPIE) Conference Series

Dicker, S. R., Korngut, P. M., Mason, B. S., Ade, P. A. R., Aguirre, J., Ames, T. J., Benford, D. J., Chen, T. C., Chervenak, J. A., Cotton, W. D., Devlin, M. J., Figueroa-Feliciano, E., Irwin, K. D., Maher, S., Mello, M., Moseley, S. H., Tally, D. J., Tucker, C., & White, S. D. 2008, in Presented at the Society of Photo-Optical Instrumentation Engineers (SPIE) Conference, Vol. 7020, Society of Photo-Optical Instrumentation Engineers (SPIE) Conference Series

Dicker, S. R., Mason, B. S., Korngut, P. M., Devlin, M. J., Ade, P. A. R., Aguirre, J., Ames, T. J., Benford, D. J., Chen, T. C., Chervenak, J. A., Cotton, W. D., , Figueroa-Feliciano, E., Irwin, K. D., Maher, S., Mello, M., & Moseley, S. H. 2009, submitted to ApJ

Gitti, M., Ferrari, C., Domainko, W., Feretti, L., & Schindler, S. 2007, A&A, 470, L25
Gómez, P. L., Loken, C., Roettiger, K., & Burns, J. O. 2002, ApJ, 569, 122
Hincks, A. D., Acquaviva, V., Ade, P., Aguirre, P., Amiri, M., Appel, J. W., Barrientos, L. F., Battistelli, E. S., Bond, J. R., Brown, B., Burger, B., Chervenak, J., Das, S., Devlin, M. J., Dicker, S., Doriese, W. B., Dunkley, J., Dünner, R., Essinger-Hileman, T., Fisher, R. P., Fowler, J. W., Hajian, A., Halpern, M., Hasselfield, M., Hernández-Monteagudo, C., Hilton, G. C., Hilton, M., Hlozek, R., Huffenberger, K., Hughes, D., Hughes, J. P., Infante, L., Irwin, K. D., Jimenez, R., Juin, J. B., Kaul, M., Klein, J., Kosowsky, A., Lau, J. M., Limon, M., Lin, Y., Lupton, R. H., Marriage, T., Marsden, D., Martocci, K., Mauskopf, P., Menanteau, F., Moodley, K., Moseley, H., Netterfield, C. B., Niemack, M. D., Nolta, M. R., Page, L. A., Parker, L., Partridge, B., Quintana, H., Reid, B., Sehgal, N., Sievers, J., Spergel, D. N., Staggs, S. T., Stryzak, O., Swetz, D., Switzer, E., Thornton, R., Trac, H., Tucker, C., Verde, L., Warne, R., Wilson, G., Wollack, E., & Zhao, Y. 2009, ArXiv e-prints
Jewell, P. R. & Prestage, R. M. 2004, in Society of Photo-Optical Instrumentation Engineers (SPIE) Conference Series, Vol. 5489, Society of Photo-Optical Instrumentation Engineers (SPIE) Conference Series, ed. J. M. Oschmann, Jr., 312–323
Kitayama, T., Komatsu, E., Ota, N., Kuwabara, T., Suto, Y., Yoshikawa, K., Hattori, M., & Matsuo, H. 2004, PASJ, 56, 17
Komatsu, E., Matsuo, H., Kitayama, T., Hattori, M., Kawabe, R., Kohno, K., Kuno, N., Schindler, S., Suto, Y., & Yoshikawa, K. 2001, PASJ, 53, 57
Markevitch, M., Gonzalez, A. H., David, L., Vikhlinin, A., Murray, S., Forman, W., Jones, C., & Tucker, W. 2002, ApJ, 567, L27
Miranda, M., Sereno, M., de Filippis, E., & Paolillo, M. 2008, MNRAS, 385, 511
Nikolic, B., Prestage, R. M., Balser, D. S., Chandler, C. J., & Hills, R. E. 2007, A&A, 465, 685
Nord, M., Basu, K., Pacaud, F., Ade, P. A. R., Bender, A. N., Benson, B. A., Bertoldi, F., Cho, H., Chon, G., Clarke, J., Dobbs, M., Ferrusca, D., Halverson, N. W., Holzapfel, W. L., Horellou, C., Johansson, D., Kennedy, J., Kermish, Z., Kneissl, R., Lanting, T., Lee, A. T., Lueker, M., Mehl, J., Menten, K. M., Plagge, T., Reichardt, C. L., Richards, P. L., Schaaf, R., Schwan, D., Spieler, H., Tucker, C., Weiss, A., & Zahn, O. 2009, A&A, 506, 623
Ota, N., Murase, K., Kitayama, T., Komatsu, E., Hattori, M., Matsuo, H., Oshima, T., Suto, Y., & Yoshikawa, K. 2008, ArXiv e-prints
Pointecouteau, E., Giard, M., Benoit, A., Désert, F. X., Aghanim, N., Coron, N., Lamarre, J. M., & Delabrouille, J. 1999, ApJ, 519, L115
Pointecouteau, E., Giard, M., Benoit, A., Désert, F. X., Bernard, J. P., Coron, N., & Lamarre, J. M. 2001, ApJ, 552, 42
Poole, G. B., Babul, A., McCarthy, I. G., Sanderson, A. J. R., & Fardal, M. A. 2008, MNRAS, 391, 1163
Reese, E. D., Carlstrom, J. E., Joy, M., Mohr, J. J., Grego, L., & Holzapfel, W. L. 2002, ApJ, 581, 53
Sazonov, S. Y. & Sunyaev, R. A. 1998, ApJ, 508, 1
Schindler, S., Guzzo, L., Ebeling, H., Boehringer, H., Chincarini, G., Collins, C. A., de Grandi, S., Neumann, D. M., Briel, U. G., Shaver, P., & Vettolani, G. 1995, A&A, 299, L9+
Schindler, S., Hattori, M., Neumann, D. M., & Boehringer, H. 1997, A&A, 317, 646
Staniszewski, Z., Ade, P. A. R., Aird, K. A., Benson, B. A., Bleem, L. E., Carlstrom, J. E., Chang, C. L., Cho, H. ., Crawford, T. M., Crites, A. T., de Haan, T., Dobbs, M. A., Halverson, N. W., Holder, G. P., Holzapfel, W. L., Hrubes, J. D., Joy, M., Keisler, R., Lanting, T. M., Lee, A. T., Leitch, E. M., Loehr, A., Lueker, M., McMahon, J. J., Mehl, J., Meyer, S. S., Mohr, J. J., Montroy, T. E., Ngeow, C. ., Padin, S., Plagge, T., Pryke, C., Reichardt, C. L., Ruhl, J. E., Schaffer, K. K., Shaw, L., Shirokoff, E., Spieler, H. G., Stalder, B., Stark, A. A., Vanderlinde, K., Vieira, J. D., Zahn, O., & Zenteno, A. 2008, ArXiv e-prints
Swetz, D. S., Ade, P. A. R., Allen, C., Amiri, M., Appel, J. W., Battistelli, E. S., Burger, B., Chervenak, J. A., Dahlen, A. J., Das, S., Denny, S., Devlin, M. J., Dicker, S. R., Doriese, W. B., Dünner, R., Essinger-Hileman, T., Fisher, R. P., Fowler, J. W., Gao, X., Hajian, A., Halpern, M., Hargrave, P. C., Hasselfield, M., Hilton, G. C., Hincks, A. D., Irwin, K. D., Jarosik, N., Kaul, M., Klein, J., Knotek, S., Lau, J. M., Limon, M., Lupton, R. H., Marriage, T. A., Martocci, K. L., Mauskopf, P., Moseley, S. H., Netterfield, C. B., Niemack, M. D., Nolta, M. R., Page, L., Parker, L. P., Reid, B. A., Reintsema, C. D., Sederberg, A. J., Sehgal, N., Sievers, J. L., Spergel, D. N., Staggs, S. T., Stryzak, O. R., Switzer, E. R., Thornton, R. J., Tucker, C., Wollack, E. J., & Zhao, Y. 2008, in Society of Photo-Optical Instrumentation Engineers (SPIE) Conference Series, Vol. 7020, Society of Photo-Optical Instrumentation Engineers (SPIE) Conference Series
Takizawa, M. 1999, ApJ, 520, 514
Vanderlinde, K., Crawford, T. M., de Haan, T., Dudley, J. P., Shaw, L., Ade, P. A. R., Aird, K. A., Benson, B. A., Bleem, L. E., Brodwin, M., Carlstrom, J. E., Chang, C. L., Crites, A. T., Desai, S., Dobbs, M. A., Foley, R. J., George, E. M., Gladders, M. D., Hall, N. R., Halverson, N. W., High, F. W., Holder, G. P., Holzapfel, W. L., Hrubes, J. D., Joy, M., Keisler, R., Knox, L., Lee, A. T., Leitch, E. M., Loehr, A., Lueker, M., Marrone, D. P., McMahon, J. J., Mehl, J., Meyer, S. S., Mohr, J. J., Montroy, T. E., Ngeow, C., Padin, S., Plagge, T., Pryke, C., Reichardt, C. L., Rest, A., Ruel, J., Ruhl, J. E., Schaffer, K. K., Shirokoff, E., Song, J., Spieler, H. G., Stalder, B., Staniszewski, Z., Stark, A. A., Stubbs, C. W., van Engelen, A., Vieira, J. D., Williamson, R., Yang, Y., Zahn, O., & Zenteno, A. 2010, ArXiv e-prints
Vikhlinin, A., Markevitch, M., & Murray, S. S. 2001, ApJ, 551, 160